Helical vortices generated by flapping wings of bumblebees

Thomas Engels[1,4], Dmitry Kolomenskiy[2], Kai Schneider[3], Marie Farge[4], Fritz-Olaf Lehmann[5] and Jörn Sesterhenn[1]

[1] *ISTA, Technische Universität Berlin, Berlin, Müller-Breslau-Strasse 12, 10623 Berlin, Germany*
[2] *Biomechanical Engineering Laboratory, Chiba University, Chiba, 1-33 Yayoi-Cho, Inage-Ku, Chiba-Shi, Chiba, 263-8522 Japan*
[3] *I2M-CNRS, Aix-Marseille Université, Marseille, 39 rue Joliot-Curie, 13451 Marseille Cedex 20 France*
[4] *LMD-CNRS, Ecole Normale Supérieure and PSL, Paris, 24 rue Lhomond, 75231 Paris Cedex 05, France*
[5] *Department of Animal Physiology, Universität Rostock, Rostock, Albert-Einstein-Str. 3, 18059 Rostock, Germany*

February 6, 2017

Abstract

High resolution direct numerical simulations of rotating and flapping bumblebee wings are presented and their aerodynamics is studied focusing on the role of leading edge vortices and the associated helicity production. We first study the flow generated by only one rotating bumblebee wing in circular motion with 45° angle of attack. We then consider a model bumblebee flying in a numerical wind tunnel, which is tethered and has rigid wings flapping with a prescribed generic motion. The inflow condition of the wind varies from laminar to strongly turbulent regimes. Massively parallel simulations show that turbulence does not significantly alter the wings' leading edge vortex (LEV), which enhances lift production. Finally, we focus on studying the helicity of the generated vortices and analyze their contribution at different scales using orthogonal wavelets.

Contents

1 Introduction

Numerical modeling of flapping insect flight receives considerable attention and is motivated by the growing interest in miniaturization of unmanned air vehicles, since flapping-wing flight is a bio-inspired alternative to fixed- and rotary-wings. Insects have wings with sharp edges, which means that the aerodynamic forces, that are necessary for flying, are typically associated with flow separation and vorticity production. Techniques for extra lift generation, like the clap-fling-sweep mechanism, are used by many insects and have been revisited in [17].

Previous research on the flow generated by flapping wings indicates the important role of the leading edge vortex [23, 4]. This vortex has a conical structure due to the three-dimensional motion of the wings. Vorticity is produced at the sharp leading edge, and outwards velocity (from the root to the tip of the wing) develops above the suction surface of the wing, see, e.g., [24, 16, 18]. Such alignment of the vorticity and the velocity has important consequences for the dynamics of the vortex. On one hand, the excess vorticity is constantly transported into the wing tip vortex rather than being shed periodically from the leading edge [24]. On the other hand, the swirl angle is large and the vortex can burst [25]. Swirling flows are characterized by strong helicity, which is defined by the scalar product of velocity and vorticity vectors and corresponds to their alignment or anti-alignment. Consideration of the helicity dynamics in flows over flapping or revolving wings can therefore bring important insights into the processes that determine the flow topology. For instance, in [13], helicity was used as a criterion to characterize bursting of the leading edge vortex on a rotating wing.

Helicity has received much attention in the topological fluid dynamics community to measure the linkage and knottedness of vortex lines in the flow. For a review we refer for instance to [28]. In the turbulence community helicity has been used to characterize three-dimensional swirling coherent structures, which correspond to flow regions of maximum helicity, see, e.g., in [9]. This local alignment or anti-alignement of velocity and vorticity implies that the nonlinear term of the Navier–Stokes equations is depleted and thus the nonlinear energy transfer is slowed down. Therefore such structures tend to persist coherently in time [29]. An example for flows with maximum helicity are Beltrami flows, which correspond to eigenfunctions of the curl operator and are hence solutions of the steady Euler equations.

To get insight into the scale disctribution of helicity we decompose the velocity and vorticity into orthogonal wavelet bases. Wavelets are localized functions in scale and space and allow analyzing flow fields efficiently. Thus the scale-dependent helicity, introduced in [34], can be computed. A review on wavelet based statistical measures for fluid and plasma turbulence can be found in [10].

The aim of this work is to examine the helicity dynamics in flows over model insect wings in connection with the effects that were previously described in terms of the vorticity and the velocity. We propose helicity as a new diagnostics to study the vortices generated by flapping and revolving wings. First, we investigate a simplified configuration of an unilaterally rotating bumblebee wing and perform high resolution numerical computations. The flow fields are studied and, in particular, the leading edge vortex is examined. Second, we analyze high resolution numerical simulation data of a flapping bumblebee flying in turbulent flow, presented in [6]. We use the orthogonal wavelet decomposition of the flow field to analyze the production of helicity at different scales, which is then quantified by the wavelet spectrum of helicity and its spatial variability.

The manuscript is organized as follows: In section 2 we describe, for reasons of self-consistency, the bumblebee model with rigid wings and the computational set-up. The wing kinematics and parameters can be found in the cited references. The numerical method, which is a Fourier pseudo-spectral method with volume penalization, is briefly recalled too. The computational results are reproducible as the "FluSI" code is open source [7]. The definition of helicity, together with its spectral decomposition and the scale-dependent helicity using orthogonal wavelets are also given. Computational results for rotating and flapping bumblebee wings are presented and subsequently analyzed in section 3. Conclusions of our findings are drawn in section 4.

2 Bumblebee model, numerical method and helicity

2.1 Bumblebee model

A model bumblebee, already used in previous work [6], is chosen among the variety of flying insects, since the flow it generates while flying remains in a range of Reynolds number which can be computed by DNS (Direct Numerical Simulation) using HPC (High Performance Computing). We consider a bumblebee (*bombus terrestris*) as typical representative for medium-size insects. Its characteristic parameters are: wing length 13.2 mm, frequency 152 Hz, mass 175 mg, and it flies, when tethered in still air conditions, at a generic Reynolds number $Re = 2060$. Bumblebees are known to be relentless all-weather foragers [33, 31] and thus encounter a wide range of flow conditions from laminar to fully turbulent [6].

2.1.1 One revolving wing

Prior to analyzing the complete insect model, we focus in this part on a commonly used reduced model, which consists of a single, revolving wing. This canonical setup is often used to study the leading edge vortex [18, 12, 11, 13]. We fix the angle of attack to $\alpha = 45°$ (i.e., the feathering angle, for details see Figure 1 and [7]). The rotation angle varies as

$$\phi(t) = \dot{\Phi}\left(\tau e^{-t/\tau} + t\right),$$

which is the same as used in previous work [18]. After a transient time, $\tau = 0.4$, the rotation angle grows linearly in time. The wingtip velocity is $u_{\text{tip}} = R\dot{\Phi}$ in the steady rotation regime. We normalize the wing length R and set $\dot{\Phi} = 1$, thus $u_{\text{tip}} = 1$. The Reynolds number is conventionally defined as $Re = u_{\text{tip}} c_m/\nu$ [22], where $c_m = A/R = 0.304$ is the mean chord length, and it is set to the same value ($Re = 2060$) as the flow generated by the tethered bumblebee flying in still air that we will study in the following sections. Note that the Reynolds number and the wingshape planform are the same as in [6]. Figure 1 (a) illustrates the setup. The wing revolves around a hinge placed at the center of a domain of size $4 \times 4 \times 2$ wing lengths, which is discretized using $1024 \times 1024 \times 512$ grid points.

2.1.2 Two flapping wings

The bumblebee flaps its wings at Reynolds numbers of approximately 2000 at forward flight speed of 2.5 m/s. We developed a 'numerical wind tunnel' and placed the animal in a $6R \times 4R \times 4R$ large, virtual rectangular box. The computational domain is discretized with 680 million grid points and the three-dimensional Navier–Stokes equations are solved by DNS on a massively parallel computer. The volume penalization method is used to handle the no-slip boundary conditions on the time-varying geometry. The mean inflow velocity accounts for the equivalent forward flight speed of the tethered insect. For simplicity we model the wings as flat rigid plates with prescribed kinematics. To model atmospheric turbulence, we use homogeneous isotropic turbulence (HIT) as turbulent inflow. HIT is characterized by the turbulent kinetic energy, the integral length scale and its Reynolds number. We vary the turbulence intensity, $Tu = u'/u_\infty$ defined as the root mean square (rms) of velocity fluctuations normalized to flight velocity, by altering the energy content of the turbulent perturbations superimposed to the mean flow. The entire procedure allows us to study insect flight from laminar to fully-developed turbulent flow regimes.

2.2 Numerical method

Numerical simulations of the flow generated by insects have to face two major challenges. First, as insects fly by flapping their wings, the geometry of the problem is complicated and varies in time, implying that the no-slip boundary condition for the Navier–Stokes equation has to be imposed on

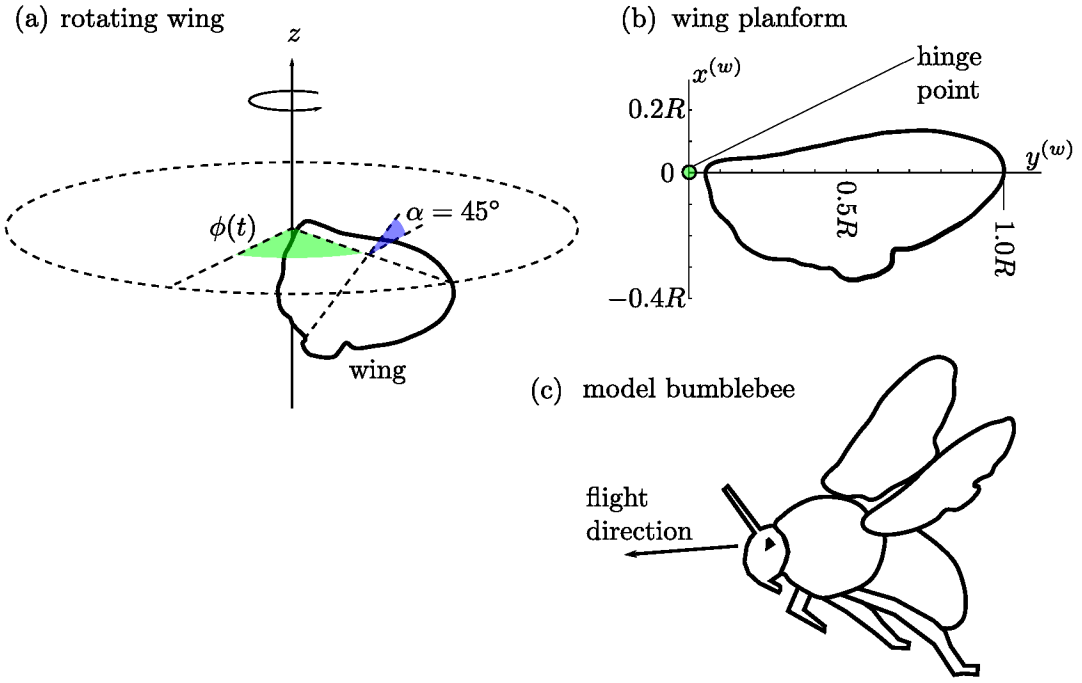

Fig. 1: Setup: configuration for the revolving wing (a),wing mask (b) and bumblebee mask (c).

a complex fluid–solid interface. Second, many insects can be typically characterized by Reynolds numbers in the intermediate regime [21, 5], i.e., $Re = \mathcal{O}\left(10^3\right)$. In this Reynolds number regime, common simplifications, such as the Stokes or inviscid approximations, are essentially nullified, leaving us with the full non-linear unsteady problem. To cope with these challenges, our numerical method combines the volume penalization method [2] with a Fourier pseudospectral discretization [32, 14], for which we developed an open–source computational environment, available on Github [7]. The code solves the incompressible, penalized Navier–Stokes equations

$$\partial_t \boldsymbol{u} + \boldsymbol{\omega} \times \boldsymbol{u} = -\nabla \Pi + \nu \nabla^2 \boldsymbol{u} - \underbrace{\frac{\chi}{C_\eta}\left(\boldsymbol{u} - \boldsymbol{u}_s\right)}_{\text{penalization}} - \underbrace{\frac{1}{C_{\text{sp}}} \nabla \times \frac{\left(\chi_{\text{sp}} \boldsymbol{\omega}\right)}{\nabla^2}}_{\text{sponge}} \tag{1}$$

$$\nabla \cdot \boldsymbol{u} = 0 \tag{2}$$

$$\boldsymbol{u}\left(\boldsymbol{x}, t=0\right) = \boldsymbol{u}_0\left(\boldsymbol{x}\right) \qquad \boldsymbol{x} \in \Omega, t > 0, \tag{3}$$

where the mask function $\chi\left(\boldsymbol{x}, t\right)$ is unity inside the insect and zero otherwise and C_η is the penalization constant. The last term is a vorticity damping term used to gradually damp vortices and alleviate the periodicity inherent to the Fourier discretization. The role of this sponge is to relaminarize the (upwind) flow as does the honeycomb in a windtunnel. Details on how the χ function and the solid body velocity field $\boldsymbol{u}_s$ are constructed can be found in [7], along with a precise description of the insect model and detailed validation tests. We use our code only to compute DNS without additional turbulence modeling, and verify via grid convergence studies that all spatial and temporal scales are resolved. The penalization parameter is set to $C_\eta = 5.66 \cdot 10^{-4}$, which means that the number of grid points in the penalization boundary layer [7] is $K_\eta = \sqrt{\nu C_\eta}/\Delta x = 0.074$. This is the same value as used in the bumblebee simulations. A sponge layer with a thickness of 32 grid points and a damping constant $C_{\text{sp}} = 0.1$ is used to damp the vorticity at the borders of the domain. For comparison, a second simulation is performed increasing the viscosity by a factor of ten, while keeping all other parameters constant. Details on the numerical code, which is open source[1], can be found in [7].

[1] https://github.com/pseudospectators/FLUSI

2.3 Helicity, helicity spectra and scale-dependent helicity

Helicity is a quantity introduced by Betchov in [3], important to study the dynamics turbulent flows. In [30, 27] is was shown that energy and helicity are two conserved quantities of the incompressible Euler equations. For a comprehensive review on helicity we refer to [28]. Considering the velocity field $\boldsymbol{u}$ and the corresponding vorticity $\boldsymbol{\omega} = \nabla \times \boldsymbol{u}$, the kinetic helicity, $H(\boldsymbol{x}) = \boldsymbol{u} \cdot \boldsymbol{\omega}$, can be defined, see, e.g., [30, 27]. The helicity yields a measure of the geometrical statistics of a turbulent flow and allows us to quantify its chirality. It changes sign when applying a mirror symmetry to the reference frame (transforming it from left to right handed). Integrating the helicity over space one obtains the mean helicity $\overline{H} = \langle \boldsymbol{u} \cdot \boldsymbol{\omega} \rangle$.

The relative helicity

$$h(\boldsymbol{x}) = \frac{H}{|\boldsymbol{u}|\,|\boldsymbol{\omega}|} \tag{4}$$

corresponds to the cosine of the angle between the velocity and the vorticity at each spatial position. The range of h thus lies between -1 and $+1$, corresponding to anti-alignment and alignment of the velocity and the vorticity vector, respectively.

Energy and helicity balance equation

Similar to the dissipation of energy (in the absence of forcing), $d_t E = -2\nu Z$ where $E = 1/2 \int |\boldsymbol{u}|^2 d\boldsymbol{x}$ and $Z = 1/2 \int |\boldsymbol{\omega}|^2 d\boldsymbol{x}$ are respectively the energy and enstrophy, mean helicity satisfies a balance equation,

$$d_t \overline{H} \;=\; -2\nu \overline{H}_\omega \tag{5}$$

where $\overline{H}_\omega = \langle \boldsymbol{\omega} \cdot (\nabla \times \boldsymbol{\omega}) \rangle$ is the mean helicity of vorticity (also called superhelicity) assuming absence of helical forcing. In viscous flows we have dissipation and generation of helicity, while in the inviscid case ($\nu = 0$) the Euler equations conserve the mean kinetic helicity. Contrary to energy neither helicity of velocity nor helicity of vorticity are positive definite quantities. The point-wise helicity $H(\boldsymbol{x}, t)$ of velocity satisfies the equation [19],

$$\partial_t H + \boldsymbol{u} \cdot \nabla H \;=\; -\nabla \cdot (\boldsymbol{\omega} p) + \frac{1}{2} \nabla \cdot (\boldsymbol{\omega} |\boldsymbol{u}|^2) + \nu (\nabla^2 H - 2(\nabla \boldsymbol{u} \nabla \boldsymbol{\omega})) \tag{6}$$

This shows that for the helicity dynamics both the nonlinear and the viscous terms locally play a role, either in enhancing or diminishing the helicity.

Energy and helicity spectrum

Computing the Fourier transform of the velocity and the vorticity, denoted by $\widehat{\cdot}$, the isotropic energy and helicity spectra can be defined,

$$E(k) \;=\; \frac{1}{2} \sum_{k=|\boldsymbol{k}|} |\widehat{\boldsymbol{u}}(\boldsymbol{k})|^2 \quad , \quad H(k) \;=\; \sum_{k=|\boldsymbol{k}|} \widehat{\boldsymbol{u}}(\boldsymbol{k}) \cdot \widehat{\boldsymbol{\omega}}(-\boldsymbol{k}) \; . \tag{7}$$

Note that $H(k)$ is also real valued, but a signed quantity, and by construction we have $\sum_{k \geq 0} E(k) = E$ and $\sum_{k \geq 0} H(k) = \overline{H}$ which justifies that $E(k)$ and $H(k)$ are called the spectral density of energy and helicity, respectively. Applying the Cauchy-Schwarz inequality, it follows that $|H(k)| \leq 2kE(k)$, which motivates the introduction of the relative helicity spectrum $|H(k)|/(2kE(k)) \leq 1$. In [19] it has been shown to fall off linearly in wave-number for large k, restoring thus the mirror symmetry of the flow at small scales in the case of isotropic turbulence.

Scale-dependent energy and helicity

Decomposing velocity and vorticity into orthogonal wavelet series, contributions at scale j can be obtained (for details see, e.g., [10]), which corresponds essentially to bandpass filtering. Those contributions are denoted by $\boldsymbol{u}_j$ and $\boldsymbol{\omega}_j$, respectively.

The scale-dependent energy can thus be defined as

$$E_j(\boldsymbol{x}) \;=\; \frac{1}{2}\,\boldsymbol{u}_j(\boldsymbol{x})\cdot\boldsymbol{u}_j(\boldsymbol{x}) \tag{8}$$

and integrating over $\boldsymbol{x}$ yields the mean energy $\overline{E}_j$ at scale 2^{-j}, which is called energy scalogram. Summing $\overline{E}_j$ (or E_j plus integration) over scale we obtain the total energy $E=\sum_j \overline{E}_j=\sum_j \langle E_j\rangle$.

Analoguously the scale-dependent helicity can be defined as

$$H_j(\boldsymbol{x}) \;=\; \boldsymbol{u}_j(\boldsymbol{x})\cdot\boldsymbol{\omega}_j(\boldsymbol{x}) \tag{9}$$

which was introduced in [34] in the context of isotropic turbulence. The scale-dependent helicity preserves Galilean invariance, though the kinetic helicity itself does not. Integrating H_j over $\boldsymbol{x}$ yields the mean helicity $\overline{H}_j$ at scale 2^{-j}, which we call helicity scalogram. The corresponding mean helicity is obtained by summing $\overline{H}_j$ (or H_j plus integration) over scale, $\overline{H}=\sum_j \overline{H}_j=\sum_j \langle H_j\rangle$, due to the orthogonality of the wavelet decomposition.

The scale-dependent relative helicity can be defined correspondingly as

$$h_j(\boldsymbol{x}) = \frac{H_j}{|\boldsymbol{u}_j|\,|\boldsymbol{\omega}_j|} \tag{10}$$

and can be used to analyze the probability distribution of the cosine of the alignment angle [34].

The scale 2^{-j} can be related to the wavenumber k_j as

$$k_j = k_\psi 2^j, \tag{11}$$

where $k_\psi=\int_0^\infty k|\hat{\psi}(k)|dk/\int_0^\infty|\widehat{\psi}(k)|dk$ is the centroid wavenumber of the chosen wavelet ($k_\psi=0.77$ for the Coiflet 12 used here). Thus the scale-dependent energy and helicity can be directly related to their corresponding Fourier spectra.

The wavelet energy spectrum can be obtained using the scalogram and eq. (11),

$$\widetilde{E}(k_j) = \frac{1}{2\Delta k_j}\langle E_j\rangle, \tag{12}$$

where $\Delta k_j=(k_{j+1}-k_j)\ln 2$ [26, 1]. It is thus directly related to the Fourier energy spectrum and yields a smoothed version [8, 26]. The orthogonality of the wavelets with respect to scale and direction guarantees that the total energy is obtained by direct summation, $E=\sum_j \widetilde{E}(k_j)$.

The wavelet helicity spectrum can then be obtained likewise

$$\widetilde{H}(k_j) = \frac{1}{2\Delta k_j}\langle H_j\rangle, \tag{13}$$

and again summation over j yields the total mean helicity. We anticipate that the wavelet helicity spectrum is a smoothed version of the Fourier helicity spectrum.

The spatial variability of the wavelet energy and helicity spectra at a given wavenumber k_j can be quantified by the standard deviation, defined as

$$\sigma[E_j]=\frac{1}{2\Delta k_j}\sqrt{\langle(\boldsymbol{u}_j\cdot\boldsymbol{u}_j)^2\rangle-(E_j)^2}\quad,\quad \sigma[H_j]=\frac{1}{2\Delta k_j}\sqrt{\langle(\boldsymbol{u}_j\cdot\boldsymbol{\omega}_j)^2\rangle-(H_j)^2}\,. \tag{14}$$

Thus the flow intermittency can be quantified. This is not possible using Fourier spectra as all spatial information is lost. The spatial variability of the energy spectrum can be related to the scale-dependent flatness, defined as the ratio of the fourth- to the second-order moment of the scale dependent velocity, as discussed, e.g., in [10]. Increasing flatness values for decreasing scale, i.e., values larger than three which are obtained for a Gaussian distribution, are attributed to the flow intermittency.

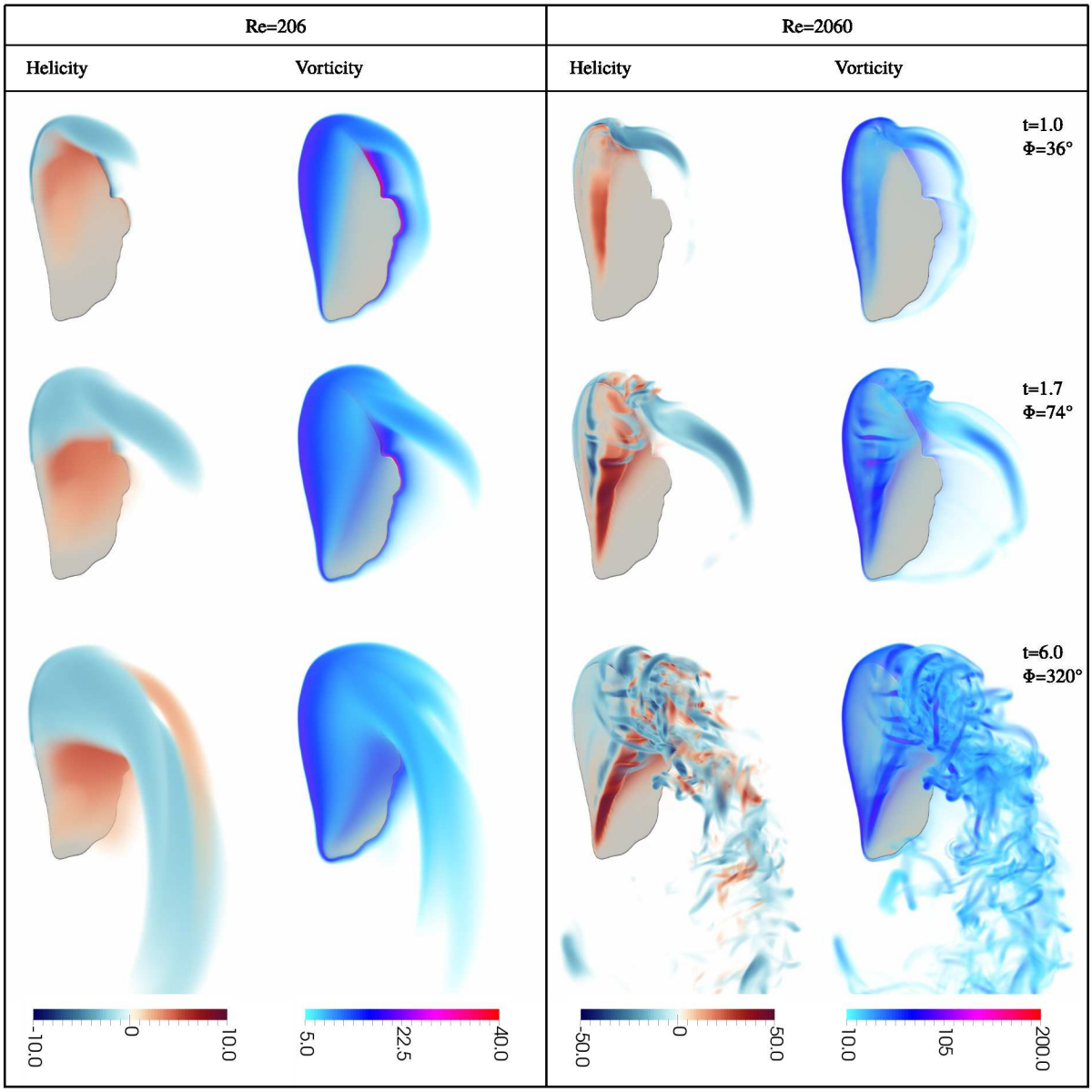

Fig. 2: Flows generated by a rotating wing at two different Reynolds numbers, $Re = 206$ (left) and 2060 (right), visualized by their helicity and vorticity magnitude at three time instants. The flow topology becomes more complex when the Reynolds number increases. Essential features, such as leading edge and tip vortices, are observed in both cases, but remain stable at $Re = 206$ and develop strong instabilities at $Re = 2060$.

.

3 Numerical results

3.1 Flow generated by a revolving bumblebee wing

This section deals with a flow generated by a bumblebee wing which steadily revolves around a hinge point with a constant angle of attack, cf. Fig. 1 (a). The general spirit is inspired by the experimental work documented in [13], where a leading edge vortex on a revolving plate is investigated. The vortex can burst but still remains attached to the wing, i.e., there is no LEV separation, and helicity can be used to characterize this bursting.

We first visualize the helicity $H(\boldsymbol{x})$ and vorticity magnitude $|\boldsymbol{\omega}(\boldsymbol{x})|$, at three different instants, for two different flows, corresponding to $Re = 206$ and 2060, respectively. For both flows the wing motion starts from rest in a quiescent fluid and a vortex is formed. The wing accelerates until $t = 0.4$ and then rotates at a constant angular velocity. Fig. 2 shows the vorticity magnitude $|\boldsymbol{\omega}(\boldsymbol{x})|$ at $t = 1.0$, which corresponds to an early phase of the steady rotation. The left box corresponds to the low Reynolds number flow and the right box to the high Reynolds number flow. In both cases, a LEV is formed, but the quantitative scale for vorticity is reduced in the viscous case. A tip vortex forms as well in both cases. The topological reconnection of the LEV and the tip vortex contains a curious transition from the positive helicity in the LEV core to the overall negative helicity in the wing tip vortex. The outwards axial flow in the LEV is driven by the centrifugal force and the axial pressure gradient produced the conical shape of the vortex. The axial flow in the wing tip vortex is created by entrainment of the fluid behind the moving wing. Consequently, the helicity changes sign near the wing tip. Later on, at $t = 6.0$, the differences in the vorticity fields of the two cases become quite remarkable, as the higher Reynolds number case develops much finer flow features near the wing tip, which are inhibited by the viscosity in the other case. It is also noted that a coherent leading edge vortex is visually less easily defined in the low viscosity case. The visualization of helicity density $h(\boldsymbol{x}) = \boldsymbol{u} \cdot \boldsymbol{\omega}$ in Fig. 2 looks qualitatively similar to the vorticity magnitude regarding the appearance of fine structures. The tip vortex is helical with a negative value of h, while the region near the root until midspan features positive values of h. In the high Reynolds case, a strongly helical leading edge vortex is visible at $t = 1.7$, which becomes incoherent towards the tip. At $t = 6.0$, more than half of the wing features an incoherent, burst leading edge vortex. We note at either Reynolds number that no vortex shedding occurs, meaning that the leading edge vortex remains attached to the wing.

This LEV bursting becomes more clearly visible when integrating the helicity density over a control volume above the suction side of the wing, where the leading edge vortex is found. This value is shown in Fig. 4 (top). From vanishing helicity due to the quiescent initial condition, the integral value $H = \int_{\Omega_{top}} \boldsymbol{u} \cdot \boldsymbol{\omega} \, \mathrm{d}V$ follows a qualitatively different evolution for the two Reynolds numbers considered. In the viscous case, H is negative throughout the simulation and builds up until around $t = 3.55$ ($\phi = 180°$), remaining constant around -0.08 afterwards. By contrast, the high Reynolds number flow first builds up positive H until a maximum is reached at $t = 1.8$ ($\phi = 81°$), then rapidly drops to a constant, negative value very close to the viscous case. The breakdown of positive helicity is a consequence of vortex bursting.

As emphasized in [13], the consequences for the force production are marginal. Figure 4 (bottom) shows both the integral force, computed as $\boldsymbol{F} = \int \chi (\boldsymbol{u} - \boldsymbol{u}_s) / C_\eta \, \mathrm{d}V$ [2], as well as the pressure contribution $\boldsymbol{F}_p = -\int \nabla p \mathrm{d}V$ for both cases. Their time evolution is qualitatively similar, and a steady force is produced after $\phi = 90°$. Figure 3 displays two-dimensional sectional plots of the vorticity magnitude, spanwise velocity magnitude and helicity density at three time instants for different spanwise positions. At $t = 1$, we observe the formation of a conical LEV core above the suction side of the wing at all three spanwise locations. Large positive spanwise vorticity in the core is collocated with the large outwards spanwise velocity, yielding large positive helicity density. In the LEV feeding sheet, however, the helicity is already changing sign from positive over the proximal part to negative over the distal part of the wing. This may be an early sign of the developing

breakdown instability. At $t = 1.7$, the proximal part of the wing still supports a compact conical core. However, the LEV core bursts over the distal part. This is seen by thickening of the core and and emergence of smaller secondary structures that wrap around the primary core. The helicity is still positive, but not as large as before the burst.

By $t = 6$, the LEV has reached its statistical equilibrium state. It begins as a laminar conical vortex from the root of the wing and bursts at around 1/3 of the wing length, forming a series of 3d strongly helical trailing vortices (ribs) which are perpendicular to the LEV.

Let us note that our results are essentially not frame dependent, because the vorticity associated with changing between the laboratory reference frame and a moving reference frame of the wing is of order 1, but the vorticity in the vortices is of order 100, i.e., two orders of magnitude larger.

Garmann and Visbal [11] point out the co-existence of the burst instability of the LEV core and the Kelvin–Helmholtz instability in the feeding LEV sheet. While the LEV burst is obvious in our numerical simulations, the Kelvin–Helmholtz instability is not apparent, possibly because the shear layer transition point is too far from the rotation axis at $Re = 2060$. The two instabilities may have different scaling with the Reynolds number, and this question needs further investigation.

Figure 5 illustrates the evolution of the relative helicity as a function of the spanwise position for $Re = 206$ (left) and $Re = 2060$ (right). The horizontal axis in each of the panels corresponds to the spanwise position r, and the vertical axis corresponds to time t. Thus, by looking at the color of a selected row of pixels on the diagram, one can see how the helicity density varies along the wing at a given t, or by looking at a selected column of pixels one can see how the helicity density at a given r varies in time.

Let us first discuss the low Re case. At startup, $t < 5$, the helicity density is negligibly small, which means that, even though some strong vorticity may be produced at the sharp edges, no significant axial flow has developed in the vortex cores. After $t = 5$, the positive helicity builds up in the LEV, and negative helicity builds up in the wing tip vortex. The wing tip vortex expands as time progresses, until saturation after $t = 30$.

At the larger Re, the diagram is similar to the extent that helicity is positive in the LEV, negative in the wing tip vortex, and the two regions develop in time until saturation at about the same time $t = 30$ and the same radial position $r = 160$. However, the magnitude of helicity is about 3 times as large as in the low-Re case. This is probably related to the enhanced axial flow in the high-Re LEV, and overall larger vorticity production in that case.

The wavelet energy spectra (Fig. 6, left) in log-log representation and helicity spectra in lin-log representation (Fig. 6, right) show the scale distribution of energy and helicity, respectively. They yield similar information as the Fourier spectra, however the wavelet spectra are less influenced by the mask function, in particular at small scales, used in the computations to impose the no-slip boundary conditions. We observe that both the energy and helicity values grow in time and that the maximum magnitude is at the same wavenumber, $k = 5$, where also a peak in the kinetic energy is observed. The corresponding standard deviations (dashed lines) illustrate the spatial fluctuations of energy and helicity. We find that small energy and helicity values at large k exhibit nevertheless large fluctuations, which is a signature of the flow intermittency.

Visualizations of the scale-wise helicity together with the energy are presented in Figure 7 at $t = 6$. The (positively) helical leading edge vortex is well visible at scales 2^{-5} and 2^{-6}, while the tip vortex, visible at larger scales, is predominantly negative. However, positively helical structure are also present in the tip vortex at all scales. Also, a negatively helical secondary LEV core is visible, adjacent to the primary positive LEV at scales 2^{-6} and 2^{-7}. The secondary core is rotating in the opposite direction to the primary core, see, e.g., [11]. Fine scaled energy contributions are located near the wing, while the far field features energy at relatively larger scales. This is not surprising, since vortical structures at smaller scales decay faster because of viscous dissipation.

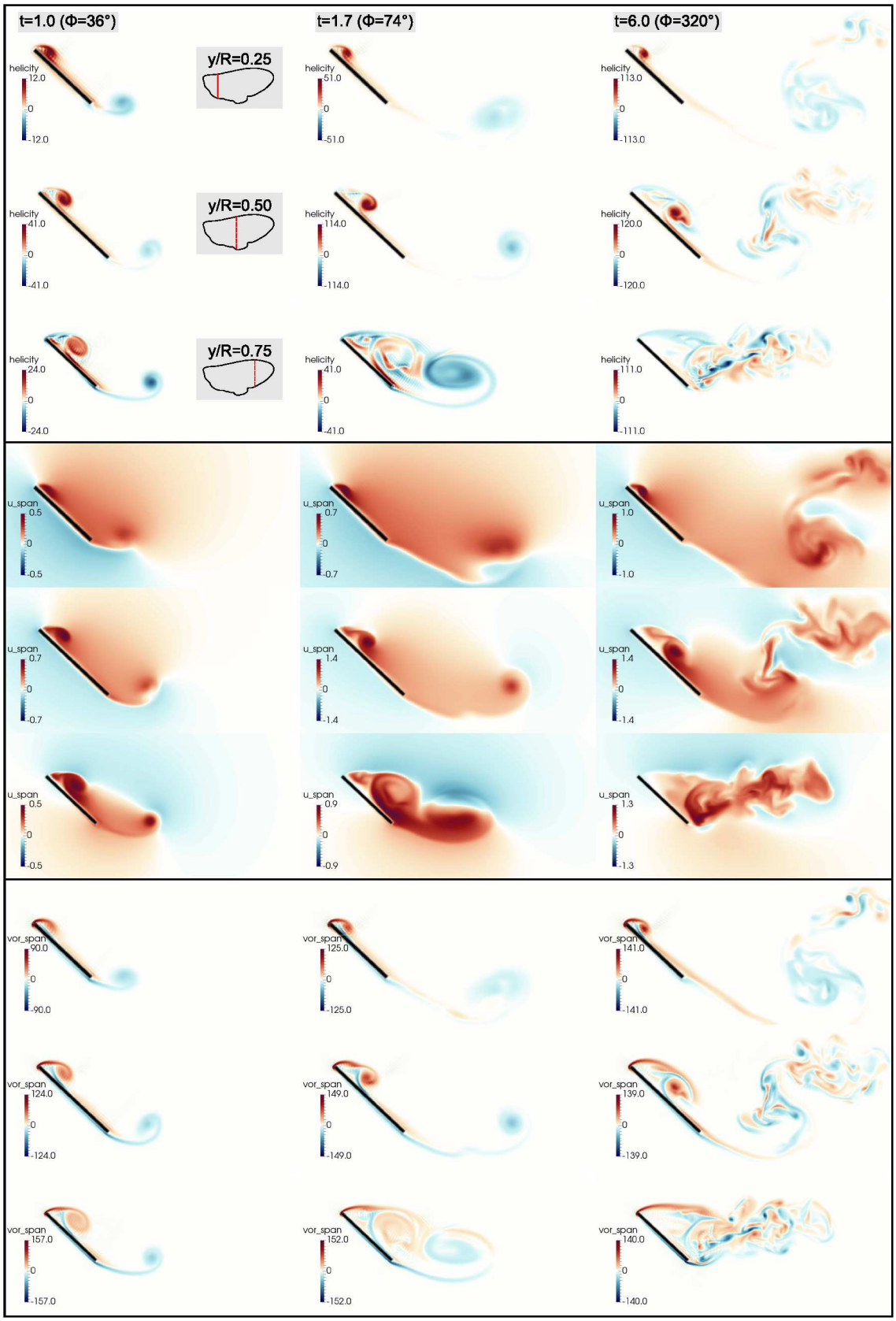

Fig. 3: Rotating wing at $Re = 2060$. Shown are two-dimensional slices of helicity (top box), spanwise velocity (middle box) and spanwise vorticity (bottom box). Slices are at three different spanwise positions, $y/R = 0.25, 0.50, 0.75$ (rows, visualized by insets in top part) and times $t = 1.0, 1.7, 6.0$ (columns).

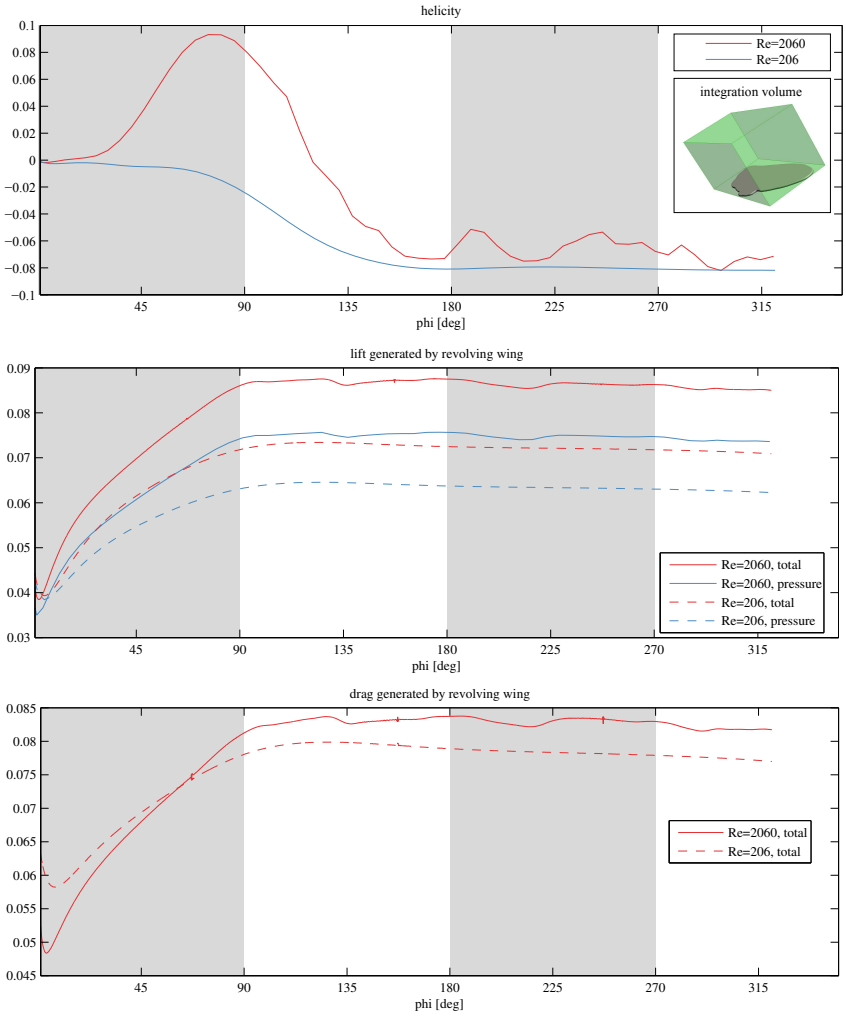

Fig. 4: Rotating wing. Time evolution of helicity, lift and drag at $Re = 206$ and 2060. Top: Helicity $H = \int_{\Omega_{top}} \boldsymbol{u} \cdot \boldsymbol{\omega} \, \mathrm{d}V$, where $\Omega_{\mathrm{top}} = [-0.35, +0.15] \times [0, 1] \times [0, 1]$ is a cubic control volume on the top surface (suction side) of the wing, as visualized by the inset. Middle: lift force is split into total and pressure contribution. The total value computed as $F_z = \int_{\Omega_s} \chi \left(\boldsymbol{u} - \boldsymbol{u}_s \right) / C_\eta \, \mathrm{d}V$ and pressure contribution $F_{pz} = - \int_{\Omega_s} \nabla p \, \mathrm{d}V$. Bottom: the corresponding drag force.

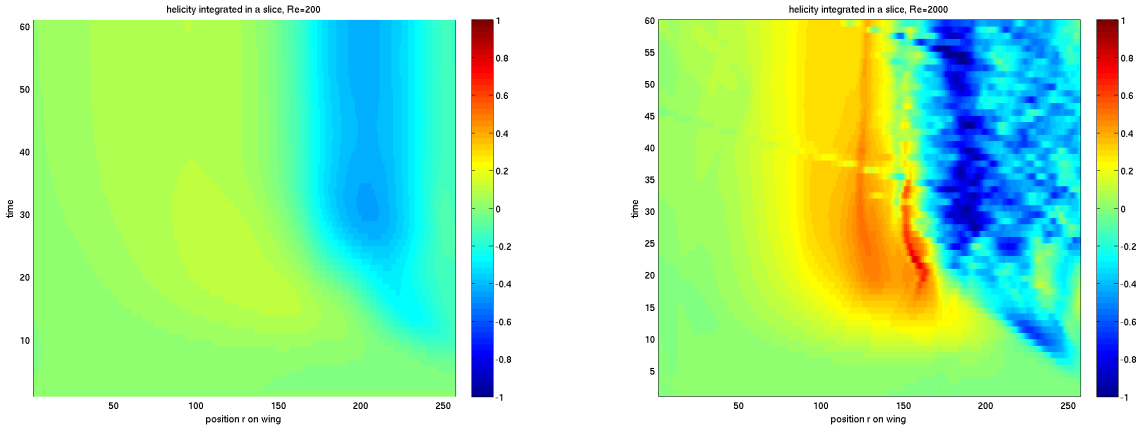

Fig. 5: Rotating wing: evolution of relative helicity, integrated in the chordwise plane, as a function of the spanwise position r on the wing, for $Re = 206$ (left) and 2060 (right).

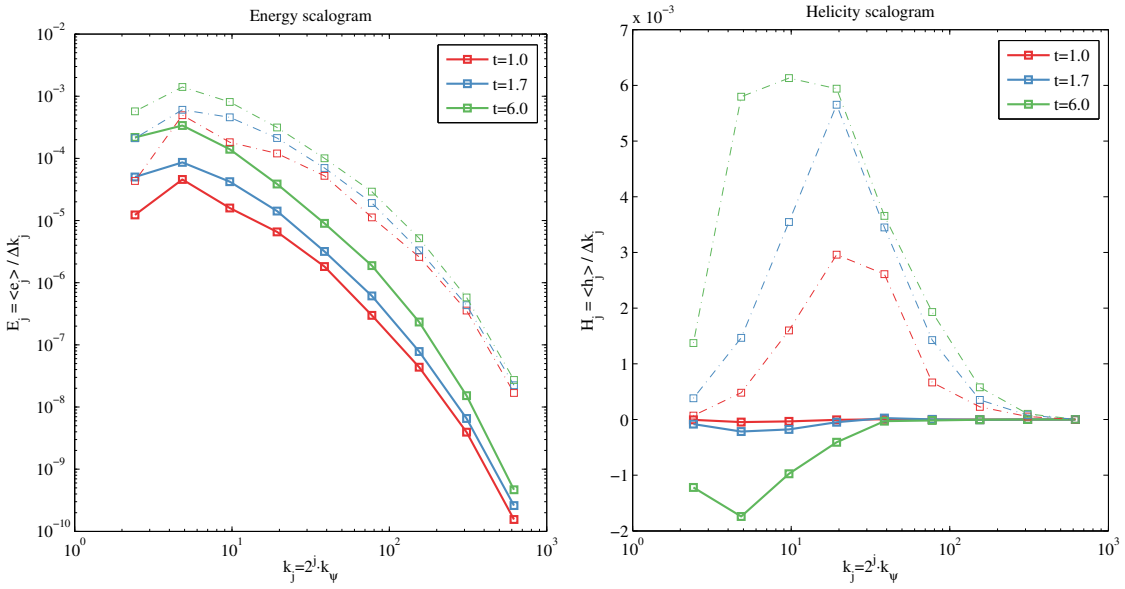

Fig. 6: Rotating wing at $Re = 2060$: Wavelet energy (left) and helicity (right) spectra (continuous lines) together with their corresponding standard deviation (dashed lines) at three different times, $t = 1.0, 1.7$ and 6.0, computed using orthogonal Coiflet 12 wavelets.

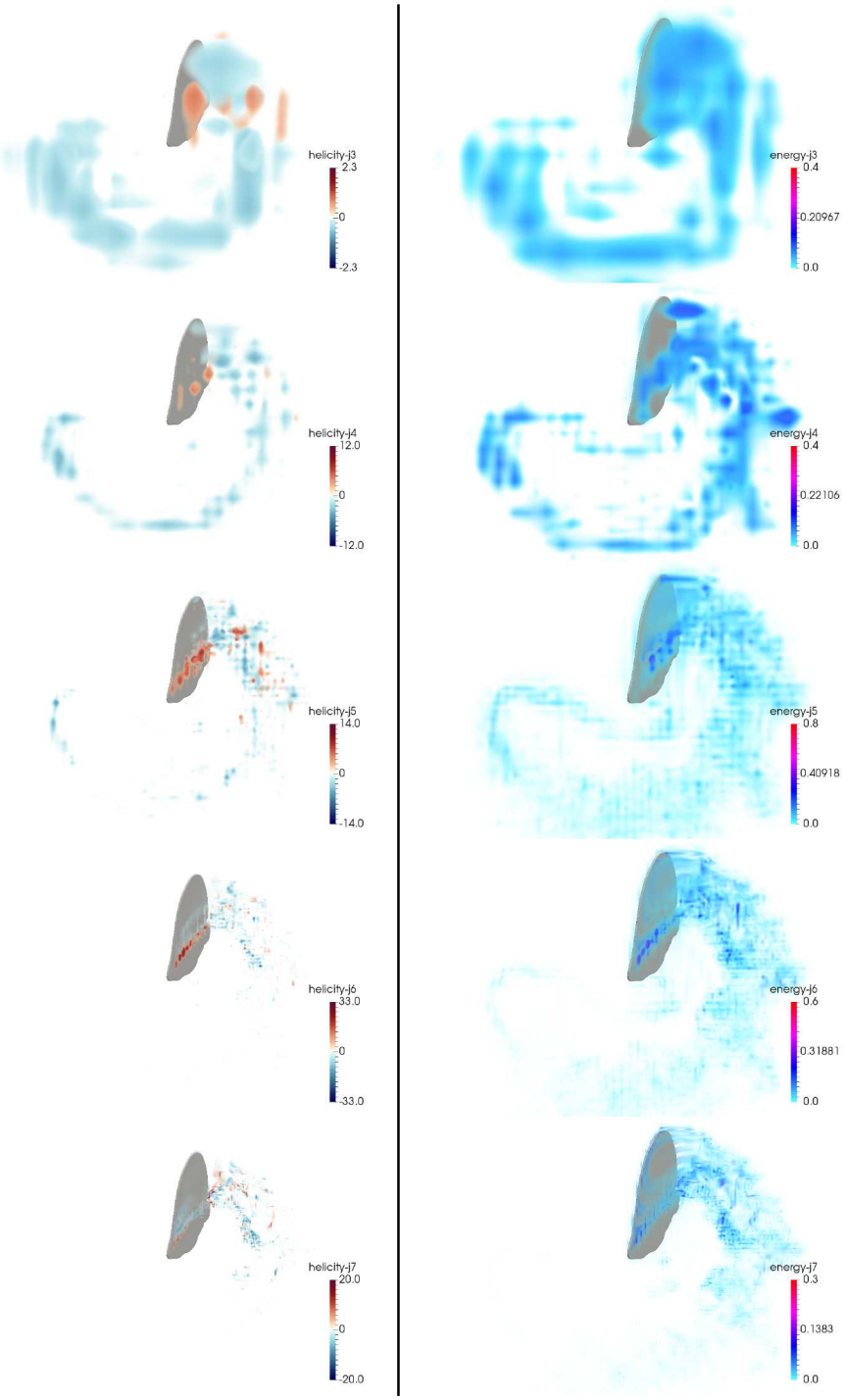

Fig. 7: Rotating wing at $Re = 2060$ and at $t = 6.0$. Helicity (left) and energy (right) visualized at four different scales from $j = 3$ (large scale) to $j = 7$ (small scale) (from top to bottom). Coiflet 12 orthogonal wavelets were used for the scale extraction.

3.2 Flow generated by the flapping wings of a tethered bumblebee

From the revolving wing studied in the previous section we now proceed to the case of a bumblebee. A key advantage of our numerical method is the simplicity with which complex geometries can be taken into account, which is why we include the insect's body in the computational model, including its legs, antennae and proboscis. For an illustration we refer to Fig. 1 (c). The body is responsible for the major part of aerodynamic drag and it may contribute, though less significantly, to the lift as well. In the interest of brevity we refer to the supplementary material of [6] for a complete description of the modeled insects morphology.

The bumblebee is considered in forward flight with a velocity of $u_\infty = 1.246$ (normalized with wing length $R = 13.2\,\mathrm{mm}$ and frequency $f = 152\,\mathrm{Hz}$), and its conventional Reynolds number is $Re = u_{\mathrm{tip}} c_m/\nu = 2060$, where $u_{\mathrm{tip}} = 2\Phi f R$ is the mean wingtip velocity and Φ the stroke angle amplitude.

A visualization of the flow fields of the bumblebee with laminar inflow is shown in Fig. 8. The vorticity magnitude illustrates the vortical structures generated by the flapping wings for a downstroke and an upstroke. To get insight into the helicity of the vortices we also show the local helicity, $h(\boldsymbol{x})$ in Fig. 8 (bottom). Positive and negative values of h correspond to alignement and anti-alignement of vorticity with velocity vectors, respectively.

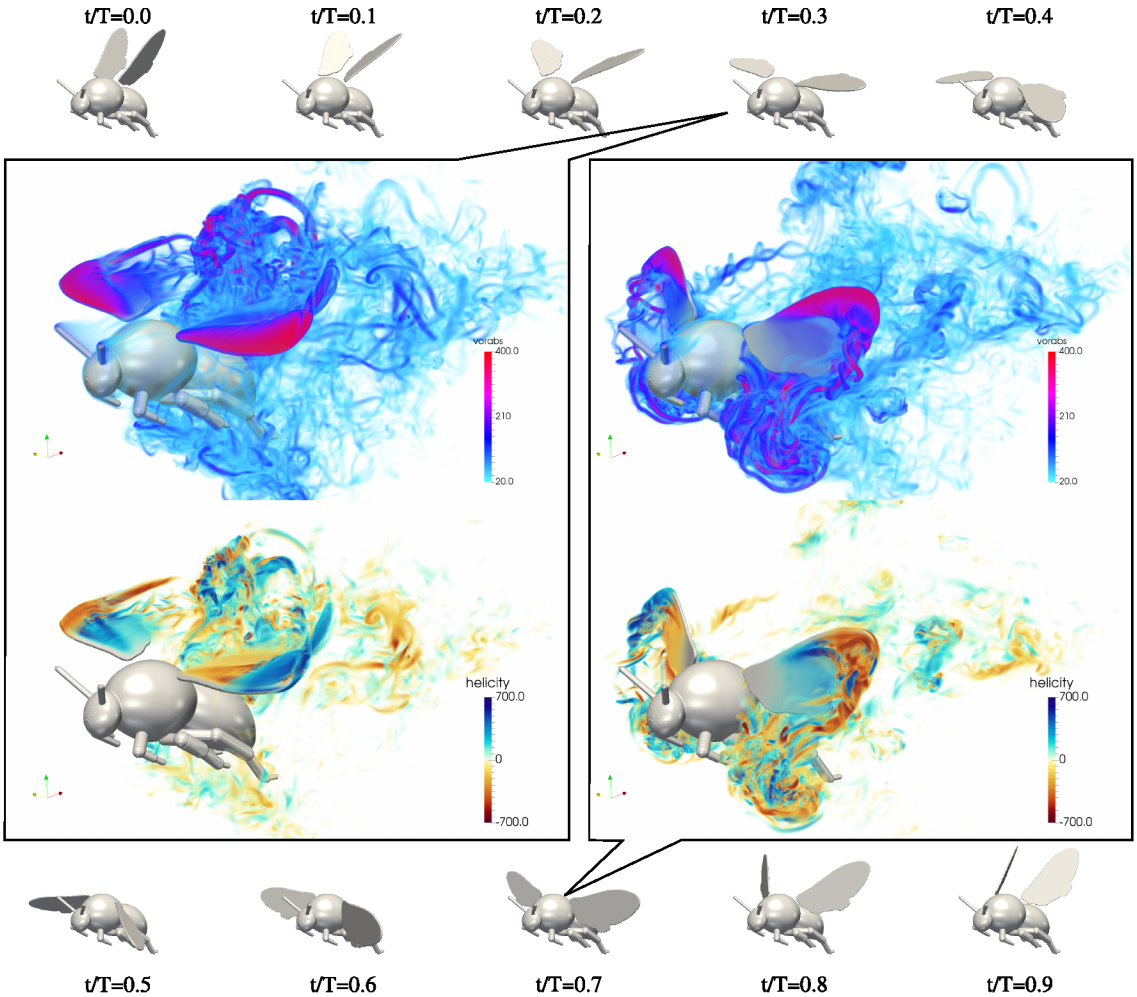

Fig. 8: Bumblebee in laminar inflow. Shown is the wingbeat kinematics for the down- (top) and upstroke (bottom). For two selected times during down- and upstroke, the flowfield is visualized by vorticity magnitude (top) and helicity (bottom). Helical leading edge vortices can be identified.

Integrating the helicity over the half-space of the computational domain with respect to the

bilateral symmetry plane of the insect, one obtains the mean helicity generated by the left and the right wing. The time evolution of both contributions is shown in Fig. 9 for laminar and turbulent inflow. We observe that the left and right wing contributions behave similarly with opposite sign and that in the turbulent case the amplitudes are much larger. Figure 9 shows time evolutions of

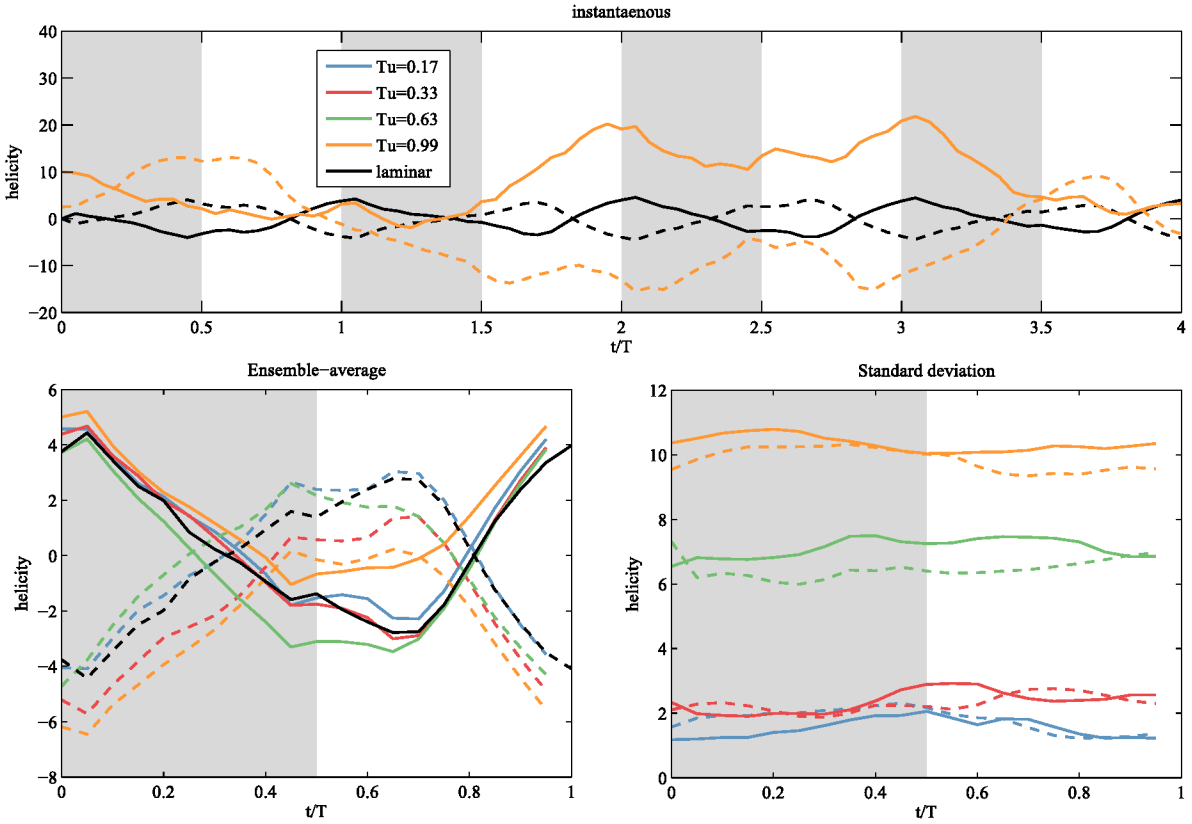

Fig. 9: Bumblebee for laminar inflow and turbulent inflow with turbulence intensity $Tu = 0.17, 0.33, 0.63$ and 0.99. Top: time evolution of the instantaneous helicity H integrated over the left and right domain with respect to the vertical center plane of the bumblebee. Bottom: time evolution of the ensemble averaged helicity H integrated over the left and right domain with respect to the vertical center plane of the bumblebee for laminar inflow and turbulent inflow (left) and corresponding standard deviation (right).

instantaneous and ensemble averaged helicity integrated over the left and right flow domain dived by the vertical center plane of the bumblebee. The motivation to consider these quantities is to analyze the generation of helicity of each wing separately. In the laminar case the sum of both instantaneous and ensemble averaged helicities is zero.

4 Conclusion

By means of high resolution direct numerical simulations we studied two flow configurations, a rotating bumblebee wing at two Reynolds numbers, and bumblebee with flapping wings considering laminar to fully turbulent inflow. We found that the leading edge vortices are helical and determined the most helical scale. The helicity increases as the Reynolds number increases, since the LEV cores become less diffuse and develop strong axial flow in the direction towards the wing tip. At the wing tip, the LEV reconnects with the wing-tip vortex, which has opposite-sign helicity at its core. As the rotation of the wing progresses in time, the LEV bursts, and its helicity reduces dramatically. However, this transition has no importance for the aerodynamic forces that remain at the same level after the burst. The analysis of a flapping bumblebee flight shows similar helical vortex structures. They are robust to the variation of the background turbulence intensity.

Acknowledgements. Financial support from the ANR (Grant 15-CE40-0019) and DFG (Grant SE 824\26 -1), project AIFIT, is gratefully acknowledged and CPU time from the supercomputer center Idris in Orsay, project i20152a1664. For this work we were also granted access to the HPC resources of Aix-Marseille Université financed by the project Equip@Meso (ANR-10-EQPX-29-01). TE, KS, MF, FL and JS thankfully acknowledge financial support granted by the ministères des Affaires étrangères et du développement International (MAEDI) et de l'Education nationale de l'Enseignement supérieur et de la Recherche (MENESR), and the Deutscher Akademischer Austauschdienst (DAAD) within the French-German Procope project FIFIT. DK gratefully acknowledges the financial support from the JSPS (Japan Society for the Promotion of Science) Postdoctoral Fellowship, JSPS KAKENHI Grant Number 15F15061.

References

[1] P.S. Addison. *The Illustrated Wavelet Transform Handbook: Introductory Theory and Applications in Science, Engineering, Medicine and Finance*. Taylor & Francis, London, 2002.

[2] P. Angot, C. Bruneau, and P. Fabrie. A penalization method to take into account obstacles in incompressible viscous flows. *Numer. Math.*, **81**:497–520, 1999.

[3] R. Betchov. Semi-isotropic turbulence and helicoidal flows. *Phys. Fluids*, **4**:925–926, 1961.

[4] C. P. Ellington, C. van den Berg, A. P. Willmott and A. L. R. Thomas. Leading edge vortices in insect flight. *Nature*, **384**, 626, 1996.

[5] C.P. Ellington. The novel aerodynamics of insect flight: applications to micro-air vehicles. *J. Exp. Biol.*, **202**:3439–3448, 1999.

[6] T. Engels, D. Kolomenskiy, K. Schneider, F.O. Lehmann and J. Sesterhenn. Bumblebee flight in heavy turbulence. *Phys. Rev. Lett.*, **116**, 028103, 2016.

[7] T. Engels, D. Kolomenskiy, K. Schneider and J. Sesterhenn. FluSI: A novel parallel simulation tool for flapping insect flight using a Fourier method with volume penalization. arXiv:1506.06513, 2015. *SIAM J. Sci. Comput.*, **38**(5), S3–S24, 2016.

[8] M. Farge. Wavelet transforms and their applications to turbulence. *Annu. Rev. of Fluid Mech.*, **24**, 395–457 (1992).

[9] M. Farge, G. Pellegrino and K. Schneider. Coherent vortex extraction in 3D turbulent flows using orthogonal wavelets. *Phys. Rev. Lett.*, **87** (5), 054501, 2001.

[10] M. Farge and K. Schneider. Wavelet transforms and their applications to MHD and plasma turbulence: a review. *J. Plasma Phys.*, **81**(6), 435810602, 2015, arXiv:1508:05650.

[11] D. J. Garmann and M. R. Visbal. Dynamics of revolving wings for various aspect ratios. *J. Fluid Mech.*, **748**:932–956, 2014.

[12] R. R. Harbig, J. Sheridan, and M. C. Thompson. Reynolds number and aspect ratio effects on the leading-edge vortex for rotating insect wing planforms. *J. Fluid Mech.*, **717**:166–192, 2013.

[13] A. R. Jones, A. Medina, H. Spooner, and K. Mulleners. Characterizing a burst leading-edge vortex on a rotating flat plate wing. *Exp. Fluids*, **57**:52, 2016.

[14] D. Kolomenskiy and K. Schneider. A Fourier spectral method for the Navier–Stokes equations with volume penalization for moving solid obstacles. *J. Comput. Phys.*, **228**:5687–5709, 2009.

[15] D. Kolomenskiy, M. Maeda, T. Engels, H. Liu, K. Schneider and J.-C. Nave. Aerodynamic ground effect in fruitfly sized insect takeoff. arXiv:1504.04484. *PLoS ONE*, **11**(3): e0152072, 2016.

[16] D. Kolomenskiy, H.K. Moffatt, M. Farge and K. Schneider. Two- and three-dimensional numerical simulations of the clap-fling-sweep of hovering insects. *J. Fluids Struct.*, **27**, 784–791, 2011.

[17] D. Kolomenskiy, H.K. Moffatt, M. Farge and K. Schneider. The Lighthill –Weis-Fogh clap-fling-sweep mechanism revisited. *J. Fluid Mech.*, **676**, 572–606, 2011.

[18] D. Kolomenskiy, Y. Elimelech and K. Schneider. Leading-edge vortex shedding from rotating wings. *Fluid Dyn. Res.*, **46**, 031421, 2014.

[19] S. Kurien, M. A. Taylor, and T. Matsumoto. Cascade time scales for energy and helicity in homogeneous isotropic turbulence. *Phys. Rev. E*, **69**,6, 066313, 2004.

[20] D. Lentink, W.B. Dickson, J.L. Van Leeuwen and M.H. Dickinson. Leading-edge vortices elevate lift of autorotating plant seeds. *Science*, **324**(5933), pp.1438-1440, 2009.

[21] P. B. S. Lissaman. Low-Reynolds-number airfoils. *Annu. Rev. Fluid Mech.*, **15**(1):223–239, 1983.

[22] H. Liu and K. Kawachi. A numerical study of insect flight. *J. Comput. Phys.*, **146**:124–156, 1998

[23] H. Liu, C.P. Ellington, K. Kawachi, C. Van Den Berg and A.P. Willmott. A computational fluid dynamic study of hawkmoth hovering. *J. Exp. Biol.*, **201**(4), 461–477, 1998.

[24] T. Maxworthy Experiments on the Weis–Fogh mechanism of lift generation by insects in hovering flight: I. Dynamics of the fling. *J. Fluid Mech.*, **93**, 47–63, 1979.

[25] T. Maxworthy The formation and maintenance of a leading-edge vortex during the forward motion of an animal wing. *J. Fluid Mech.*, **587**, 471–475, 2007.

[26] C. Meneveau. Analysis of turbulence in the orthonormal wavelet representation. *J. Fluid Mech.*, **232**, 469, 1991.

[27] H.K. Moffatt. The degree of knottedness of tangled vortex lines. *J. Fluid Mech.* , **35**, 117–129, 1969.

[28] H.K. Moffatt and A. Tsinober. Helicity in laminar and turbulent flow. *Annu. Rev. Fluid Mech.*, **24**, 281–312, 1992.

[29] H.K. Moffatt. Helicity and singular structures in fluid dynamics. *Proc. Natl. Acad. Sci. U. S. A.*, **111**(10), 3663–3670, 2014

[30] J. J. Moreau. Constantes d'un îlot tourbillonnaire en fluid parfait barotrope. *C.R. Acad. Sci. Paris*, **252**, 2810–2812, 1961

[31] S. Ravi, J.D. Crall, A. Fisher, and S. A. Combes. Rolling with the flow: bumblebees flying in unsteady wakes. *J. Exp. Biol.*, **216**:4299–4309, 2013.

[32] K. Schneider. Numerical simulation of the transient flow behaviour in chemical reactors using a penalisation method. *Computers & Fluids*, **34**:1223–1238, 2005.

[33] T. J. Wolf, C. P. Ellington, and I. S. Begley. Foraging costs in bumblebees: field conditions cause large individual differences. *Insectes Sociaux*, **46**(3):291–295, 1999.

[34] K. Yoshimatsu, N. Okamoto, K. Schneider, Y. Kaneda and M. Farge. Intermittency and scale-dependent statistics in fully developed turbulence. *Phys. Rev. E*, **79**, 026303, 2009.